Modeling Multicomponent Gas Separation Using Hollow-Fiber Membrane Contactors

D. T. Coker and B. D. Freeman
Dept. of Chemical Engineering, North Carolina State University, Raleigh, NC 27695

G. K. Fleming
Air Liquide, Newport, DE 19804

A model developed for multicomponent gas separation using hollow-fiber contactors permits simulation of cocurrent, countercurrent, and crossflow contacting patterns with permeate purging (or sweep). The numerical approach proposed permits simulation to much higher stage cuts than previously published work and provides rapid and stable solutions for cases with many components, with widely varying permeability coefficients. This new approach also permits the rational and straightforward incorporation of effects such as permeate sweep, pressure-dependent permeability coefficients, and bore side pressure gradients. Simulation results are presented for separation of commercially significant multicomponent gas mixtures using polymer permeation properties similar to those of polysulfone. The effect of permeate purging on separation performance is explored for air separation. The influence of pressure ratio on hydrogen separation performance for a refinery stream is presented. Air is modeled as a four-component mixture of O_2, N_2, CO_2, and H_2O and the refinery stream contains five components: H_2, CH_4, C_2H_4, C_2H_6, and C_3H_8. In air separation, permeate purging with a small fraction of the residue stream provides a very effective method for improving module efficiency for drying but is not efficient for improving nitrogen purity or recovery. In multicomponent mixtures, maxima in the compositions of components of intermediate permeability may be observed as a function of distance along the hollow fiber. This result suggests the use of membrane staging to capture these components at their maximum concentration.

Introduction

The use of polymeric membranes for gas separation is becoming a standardized unit operation for several applications. One of the earliest commercial applications using membranes was related to hydrogen recovery from ammonia purge gas (Maclean et al., 1980). Membrane-based hydrogen separation from mixtures of gases containing components such as methane, carbon monoxide, and nitrogen continues to be important in industrial applications such as syngas (H_2/CO) ratio adjustment (Zolandz and Fleming, 1992) and hydrogen recovery from hydrocarbons in refineries and petrochemical processes (Bollinger et al., 1984). Membrane-based air separation is used to produce nitrogen at concentrations as high as 99.5%, but membranes are most efficient producing N_2 in the 99.9% purity range (Spillman, 1989). The production of nitrogen-enriched air-using membranes is important in inert gas blanketing of fresh fruits and vegetables and inflammable liquids (Spillman, 1989). Raw natural gas frequently contains impurities such as carbon dioxide and hydrogen sulfide which must be removed prior to delivery by pipelines (Spillman, 1989). Both carbon dioxide and hydrogen sulfide are much more permeable than methane, enabling concentrated methane to be recovered as a high-pressure stream using membrane processes (Spillman, 1989). Dehydration of natural gas occurs simultaneously with CO_2 removal since water is typically highly permeable. Reduction

Correspondence concerning this article should be addressed to B. D. Freeman.
Current address of D. T. Coker: Air Liquide, 2700 Post Oak Boulevard, Suite 1800, Houston, TX 77056.

in the water vapor driving force due to concentration polarization at the downstream surface can be minimized by providing a dry gas sweep at ambient pressure at the downstream side (Zolandz and Fleming, 1992). Usually, a part of the dry gas produced by the membrane is used as the sweep (Zolandz and Fleming, 1992). In addition to dehydration of natural gas, air can be dehydrated using membrane systems, and such systems supply dry air for small laboratory and instrumentation applications (Wang et al., 1992). The recovery of volatile organic compounds from mixtures with air or other permanent gases such as methane or hydrogen is a recently commercialized membrane-based separation used for removing low levels of condensable organics from gas streams employing novel, vapor-selective membrane materials (Baker et al., 1987; Freeman and Pinnau, 1997; Morisato et al., 1996). Such membrane systems are used to recover vinyl chloride monomer from (polyvinyl chloride) reactor vent streams, chlorofluorocarbons from coating operations, and ethylene and propylene from purge bin off-gas streams in the production of polyethylene and polypropylene.

In each of the applications described above, models are required to predict the performance of gas separation modules for process design and optimization. For the current study as well as for many of the modeling studies in the literature, hollow-fiber membrane modules are the focus of the modeling efforts due to their widespread industrial use for membrane-based gas separation.

Excellent reviews of existing models of membrane gas permeators are presented by Kovvali et al. (1992) and by Lipscomb (1996). For highly simplified cases (such as perfectly mixed residue and feed), analytical solutions are available (Naylor and Backer, 1955; Smith et al., 1996; Weller and Steiner, 1950). Solutions for more complex cases are generally obtained by series approximations or asymptotic analyses of the underlying differential equations governing mass-transfer and pressure distribution in the module (Basaran and Auvil, 1988; Boucif et al., 1984; Krovvidi et al., 1992) or by solving the governing differential equations directly as a two point boundary value problem using shooting techniques (Kovvali et al., 1992).

This study presents a multicomponent model that permits rapid solution of the governing differential mass and pressure distribution in a hollow-fiber gas separation contactor using a computational scheme that does not rely on conventional shooting techniques, which may be unstable, for numerical integration. Our numerical scheme permits rapid resolution of the differential mass and pressure distribution equations even at very high stage cuts ($> 95\%$) for mixtures containing multiple components and wide variations in component permeances. The model is developed for countercurrent, cocurrent, and cross-flow contacting patterns with or without permeate purging. Results presented for air separation show the effect of permeate purging on nitrogen purity and recovery, as well as H_2O dew point of residue gas. In multicomponent mixtures, the composition of components of intermediate permeability may go through a maximum with position in the contactor, and this phenomenon is presented and discussed.

Mathematical Model

Figure 1 shows the flow configuration and internal structure of a typical hollow-fiber gas separation module. The hollow fiber bundle is sealed on both ends by epoxy tubesheets and is contained inside a high-pressure housing. Feed gas may be introduced on the bore of the hollow fibers (as shown in Figure 1) or on the shell side of the module. For air separation, bore side feed is commonly used commercially. For hydrogen separations such as the refinery applications discussed in this work, transmembrane pressures are much greater and shell side feed is common.

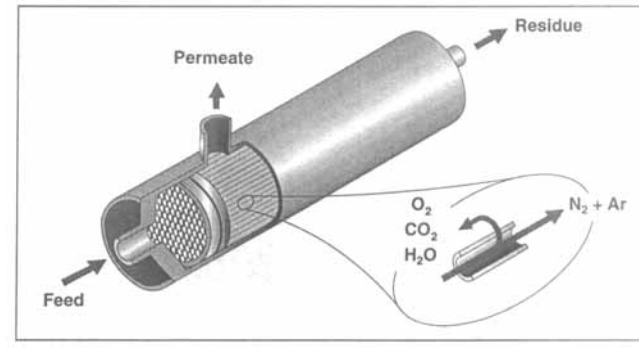

Figure 1. Hollow-fiber module.

Typically, a set of coupled, nonlinear differential equations are solved to determine mole fractions of each component in the feed and permeate, pressure in the fiber lumen (that is, the bore of the hollow fiber) and in the module shell, and feed and permeate flow rate as a function of axial position along the length of the hollow fiber module. The resulting set of $2(R-1)+4$ differential equations (where R is the number of components in the feed) together with specified feed flow rate, feed pressure, feed composition, and permeate outlet pressure form a two point boundary value problem. Many examples in the literature describe so-called "shooting" techniques to solve this problem iteratively (Kovvali et al., 1992). However, this methodology becomes cumbersome when there are more than two components, when the permeability coefficients are functions of pressure and composition, and when temperature effects are included. These techniques can be unstable when calculations are performed at very high permeate recoveries of one or more components. For these reasons, we have adopted an alternative strategy which is not based on the standard shooting techniques. The present treatment provides a simple, flexible framework for modeling the separation of multicomponent mixtures and permits the rapid implementation of effects such as expansion-driven heating or cooling of the gas mixture and pressure, composition, and temperature-dependent permeability coefficients.

The principal assumptions underpinning the model are:

(1) Shell side pressure change is negligible.

(2) Bore side pressure change is given by the Hagen-Poiseuille equation.

(3) The hollow fibers consist of a very thin membrane separation layer on a porous support as shown in Figure 2. All mass-transfer resistance is confined to the separation membrane or the total membrane wall.

(4) There is no axial mixing of shell or lumen side gases in the direction of bulk gas flow.

(5) The gas on the shell side of the hollow fibers and in the lumen is in plug flow.

(6) The performance of a single hollow fiber is calculated in the simulation and these results are scaled in proportion

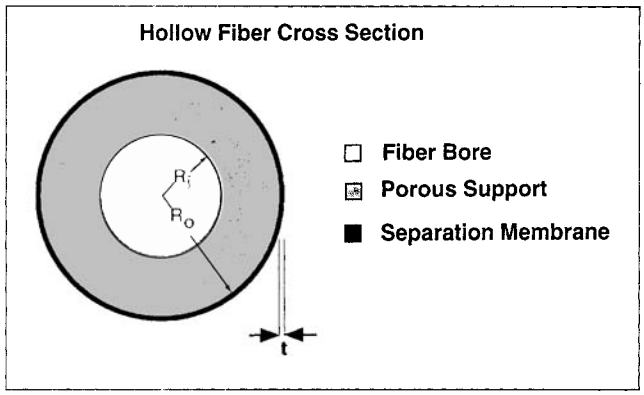

Figure 2. Hollow-fiber cross section of inside diameter $2R_i$, outside diameter $2R_o$ and dense separating layer effective thickness t.

to the number of fibers in the module to account for total gas flow and membrane area.

(7) The deformation of the hollow fiber under pressure is negligible.

(8) All fibers have uniform inner and outer radius as well as a uniform thickness separation membrane.

(9) The membrane module is operated at steady state.

As explained in more detail in the following sections, the representative hollow fiber is divided into a series of N stages in the axial direction and mass balances are enforced in each section. This procedure is formally equivalent to using first-order finite differences to develop a set of coupled difference equations from the differential mass balances for this problem. The differential mass and pressure distribution equations have been published previously (Lipscomb, 1996; Pan, 1986).

Countercurrent flow

Figure 3a shows the membrane module broken into a series of N perfectly mixed countercurrent stages. For hollow fibers, the membrane area is divided into N equal area increments

$$\Delta A_k = \frac{2\pi R_o L N_f}{N} \tag{1}$$

where L is the active (or permeating) length of the hollow fibers in the module (m), N_f is the number of fibers in the module, and R_o is the outer radius (m) of the hollow fiber, as shown in Figure 2. In Figure 3a, L_k and V_k are the total feed and permeate flow rates leaving stage k (kmol/s). The mole fractions of component j leaving the feed and permeate sides of the membrane at stage k are $x_{j,k}$ and $y_{j,k}$, respectively. The flow rates of component j leaving stage k (kmol/s) on the high- and low-pressure sides of the membrane are $\ell_{j,k}$ and $v_{j,k}$, respectively. Species mole fractions, component flow rate, and total flow rates are related as follows

$$\ell_{j,k} = x_{j,k} L_k \tag{2}$$

$$v_{j,k} = y_{j,k} V_k \tag{3}$$

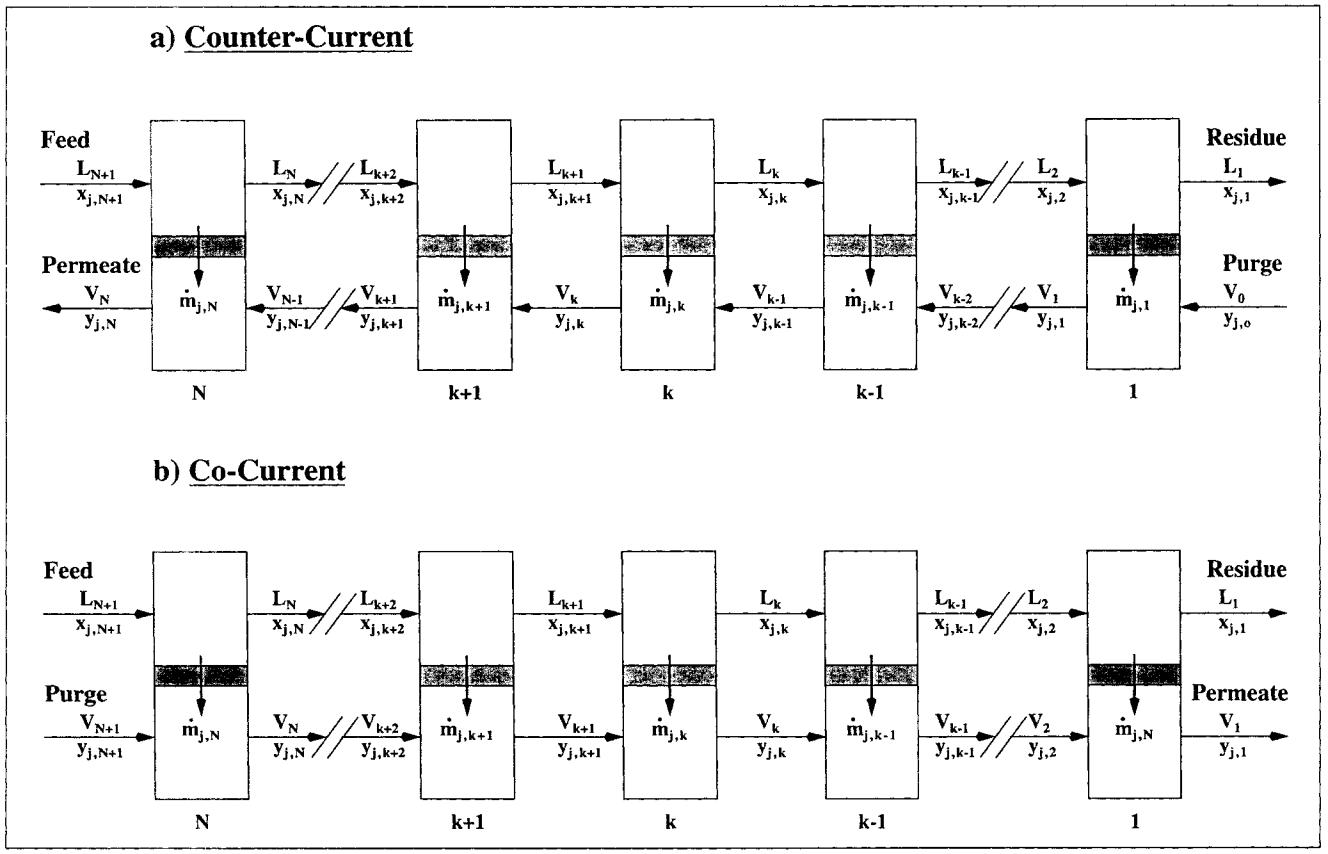

Figure 3. Module divided into N sections: (a) countercurrent; (b) cocurrent.

The total feed and permeate flow rates on stage k are the sum of the component flow rates as shown below

$$L_k = \sum_{j=1}^{R} \ell_{j,k} \tag{4}$$

$$V_k = \sum_{j=1}^{R} v_{j,k} \tag{5}$$

where R is the number of components. A component j mass balance over stage k yields

$$\ell_{j,k+1} - \ell_{j,k} + v_{j,k-1} - v_{j,k} = 0 \tag{6}$$

The transport of component j from the feed to permeate stream as a result of permeation across the membrane on stage k is

$$\dot{m}_{j,k} = \ell_{j,k+1} - \ell_{j,k} \tag{7}$$

where $\dot{m}_{j,k}$ is the mass-flow rate of component j that leaves stage k (kmol/s) due to permeation through the membrane. The mass-flow rate is given by Barrer et al. (1962), Ghosal and Freeman (1994), and Graham (1866)

$$\dot{m}_{j,k} = Q_j \Delta A_k (P_{L_k} x_{j,k} - P_{V_k} y_{j,k}) \tag{8}$$

where Q_j is the permeance (that is, permeability divided by active layer membrane thickness) of component j (kmol/(m^{2}sPa)), ΔA_k is the area available for mass transfer on stage k (m^2), and P_{L_k} and P_{V_k} are the feed and permeate pressures on stage k (Pa). Equations 2 and 3 may be used to eliminate the component mole fractions from Eq. 8 which, when combined with Eq. 7 to eliminate $\dot{m}_{j,k}$, can be rearranged as follows to provide an expression for $v_{j,k}$:

$$v_{j,k} = \frac{-V_k}{P_{V_k} \Delta A_k Q_j} \left[\ell_{j,k+1} - \left(1 + \frac{Q_j \Delta A_k P_{L_k}}{L_k} \right) \ell_{j,k} \right] \tag{9}$$

Because the permeate pressure appears in the denominator of Eq. 9, this model must be reformulated for problems in which the downstream partial pressure of component j is zero (that is, vacuum downstream). However, in these instances, the countercurrent model reduces to the cross-flow model discussed below. Equation 9 may be introduced into Eq. 6 to eliminate $v_{j,k}$ and $v_{j,k-1}$ to yield the following expression

$$B_{j,k} \ell_{j,k-1} + C_{j,k} \ell_{j,k} + D_{j,k} \ell_{j,k+1} = 0 \tag{10}$$

where the coefficients $B_{j,k}$, $C_{j,k}$, and $D_{j,k}$ are

$$B_{j,k} = \frac{-V_{k-1}}{P_{V_{k-1}} \Delta A_{k-1} Q_j} \left(1 + \frac{Q_j \Delta A_{k-1} P_{L_{k-1}}}{L_{k-1}} \right) \tag{11}$$

$$C_{j,k} = 1 + \frac{V_{k-1}}{P_{V_{k-1}} \Delta A_{k-1} Q_j} + \frac{V_k}{P_{V_k} \Delta A_k Q_j} \left(1 + \frac{Q_j \Delta A_k P_{L_k}}{L_k} \right) \tag{12}$$

$$D_{j,k} = \frac{-V_k}{P_{V_k} \Delta A_k Q_j} - 1 \tag{13}$$

In applying these coefficients to the first stage (that is, $k = 1$), V_o is the flow rate of the sweep (or permeate purge) stream. For component j, Eq. 10 can be written for each stage to yield a set of N simultaneous equations. These equations may be organized to form a tridiagonal matrix as follows

$$\begin{bmatrix} C_{j,1} & D_{j,1} & & & & \\ B_{j,2} & C_{j,2} & D_{j,2} & & & \\ & \ddots & \ddots & \ddots & & \\ & & B_{j,k} & C_{j,k} & D_{j,k} & \\ & & & \ddots & \ddots & \ddots \\ & & & B_{j,N-1} & C_{j,N-1} & D_{j,N-1} \\ & & & & B_{j,N} & C_{j,N} \end{bmatrix} \begin{bmatrix} \ell_{j,1} \\ \ell_{j,2} \\ \ell_{j,k} \\ \ell_{j,N-1} \\ \ell_{j,N} \end{bmatrix} = \begin{bmatrix} -B_{j,1} \\ 0 \\ 0 \\ 0 \\ -D_{j,N} \end{bmatrix} \tag{14}$$

Tridiagonal matrices may be solved very efficiently using the Thomas algorithm (King, 1980). The solution to Eq. 14 yields the feed side flow rates of component j on each of the N membrane stages.

Once the component flow rates are calculated for each stage on the feed side, the total feed side flows are calculated from Eq. 3. The permeate side flow rates at each stage is calculated as follows

$$V_k = V_{k-1} + L_{k+1} - L_k \tag{15}$$

From the solution to the tridiagonal matrix for each component, improved estimates of the component flow rates on each stage are obtained. These values are used to recompute values of the coefficients in Eqs. 11–13, and the tridiagonal matrices are resolved to provide better estimates of component flow rates. This successive approximation procedure is repeated until the following criteria are met

$$\left| \frac{\Delta L_1}{L_1} \right| < 10^{-8} \tag{16}$$

and

$$\left| \frac{\Delta V_{N+1}}{V_{N+1}} \right| < 10^{-8} \tag{17}$$

where ΔL_1 and ΔV_{N+1} are the changes in total residue flow and total permeate flow from one iteration to the next.

To use this method, an initial guess must be provided for the component flow rates on each stage since the coefficients in Eqs. 11–13 depend on flow rates on each stage. A cross-flow simulator provides initial estimates for the component flow rates on each stage. In cross-flow (as demonstrated be-

low), the composition of gas produced on a stage depends only on the upstream compositions, permeances, and upstream and downstream pressure. That is, the permeate composition on a stage is independent of the composition of gas produced downstream by permeation in other stages. For this reason, the cross-flow model is straightforward and rapid to solve. Moreover, by treating the module as a series of cross-flow stages, the variation in residue side gas concentration with position in the module is introduced, which provides a much more accurate initial guess for the countercurrent simulator than simpler models, such as the complete mixing model. In the cross-flow model, the mole fraction of component j produced on stage k is given by (Shindo et al., 1985)

$$y_{j,k} - \frac{Q_j(P_{L_k}x_{j,k} - P_{V_k}y_{j,k})}{\sum_{m=1}^{R} Q_m(P_{L_k}x_{m,k} - P_{V_k}y_{m,k})} = 0 \qquad (18)$$

From Eq. 18, a set of $R-1$ independent algebraic equations may be written for the compositions on each stage. Beginning at the feed end of the module, these equations are solved simultaneously using Newton's method to give the composition of permeate gas produced in each stage. For all stages except stage N (the feed stage), the initial guesses of permeate composition required by Newton's method are given by the composition of permeate gas produced on the previous stage. For stage N, the initial guesses of $y_{j,N}$ for components 1, 2, 3, ..., $R-1$ are provided by (Geankoplis, 1993)

$$y_{j,N} = \frac{Q_j x_{j,N+1}}{\sum_{m=1}^{R} Q_m x_{m,N+1}} \qquad (19)$$

which represents the solution to Eq. 18 in the limit when the ratio of feed to permeate pressure is much greater than membrane selectivity (that is, selectivity limited separation). If Eq. 19 predicts that the partial pressure of any component in the permeate is greater than its partial pressure in the feed, then the composition of that component is estimated by (Geankoplis, 1993)

$$y_{j,N} = x_{j,N}\frac{P_{L_N}}{P_{V_N}} \qquad (20)$$

which is the maximum possible permeate purity when selectivity is much greater than the ratio of feed to permeate pressure (that is, pressure ratio limited separation). This limit corresponds to the case when the partial pressure of each component is equal in the permeate and feed and, therefore, the driving force for further mass transfer is zero (Geankoplis, 1993). If the sum of the mole fractions of all permeate components on stage N are greater than one, the guessed permeate compositions are renormalized to unity.

From Eq. 8, the amount of permeate gas produced on each stage may be calculated. From these results, the change in residue flow rate from stage to stage is calculated using Eq. 7. The total permeate gas composition and flow rate are computed from the compositions and flow rates on each stage.

The pressure on the shell side of the fibers is generally taken to be constant and equal to the feed pressure. As is customary for hollow-fiber membrane separator models (Kovvali et al., 1992; Lipscomb, 1996), the tube-side (that is, permeate) pressure change from stage to stage is calculated using the Hagen-Poiseuille relation for laminar flow of an incompressible fluid in an impermeable tube (Bird et al., 1960)

$$P_{V_{k-1}} - P_{V_k} = \frac{8\mu_{\text{mix}}}{\pi R_i^4} V_k \frac{RT}{P_{V_k}} \Delta z \qquad (21)$$

where μ_{mix} is the gas mixture viscosity (Pa·s), which is computed using the Wilke equation (Bird et al., 1960), R_i is the inner radius of the hollow fiber (m), and Δz is the length of fiber in the stage (m) ($\Delta z = L/N_f$). After calculating and updating the mass flow by the procedure outlined above, the bore side pressure profile is recomputed using Eq. 21 and the updated flow rates at each stage. For bore-side feed V_k is replaced by L_k, P_{V_k} on the righthand side is replaced by P_{L_k}, and $P_{V_{k-1}} - P_{V_k}$ is replaced by $P_{L_{k+1}} - P_{L_k}$.

As these membrane units are used to separate compressible gas mixtures and the hollow fibers are permeable, one could modify Eq. 21 to account for the effects of gas compressibility and fiber permeability on lumen pressure profile. This modification is straightforward and is presented in the Appendix. As shown by the example calculations in the Appendix, for the simulation cases presented in this study, the influence of gas compressibility and gas flow through the side walls of the fibers on the lumen pressure profile are negligible.

In order to perform a simulation, a value for the number of stages N must be selected. This value is important since selecting too few stages will lead to inaccuracies in the solution and selecting too many stages will result in simulations requiring more computer time than necessary. We select N based on a conservative estimate of the number of stages needed to accurately represent the composition profile of each component. We use Eqs. 1, 7, and 8 for this calculation. The permeate pressure is set to zero in Eq. 8, since the largest amount of mass transfer will occur if the downstream partial pressure is zero. The upstream pressure is set equal to the feed pressure P_F (Pa) since this gives the highest driving force for mass transfer. We calculate the area in a single stage of the separator which would allow a maximum change in the mole fraction of each component $\Delta x_{\max}$ away from its value in the feed x_{F_j}. With these conditions, we set Eq. 7 equal to Eq. 8 and introduce Eq. 1 to obtain

$$N = \frac{2\pi R_o L N_f (1 - x_{F_j} + \Delta x_{\max}) Q_j P_F x_{F_j}}{F \Delta x_{\max}} \qquad (22)$$

In the simulations presented in this study, the value of $\Delta x_{\max}$ is 0.005. Reducing $\Delta x_{\max}$ below this value never significantly changed the computed compositions, flow rates, or pressures. We use Eq. 22 to calculate a value of N for each component and use the maximum number in subsequent calculations. This maximum number was rounded up to the nearest 100 stages. Most simulation results were obtained using $N = 100$, the minimum value. For some cases, when the stage cut was

extremely high (> 90%), the required number of stages was as large as 1,000. For cases with widely varying feed compositions and permeabilities, one could also set Δx_{max} to a fraction of the feed composition rather than an absolute number.

The cross-flow model generally provides an excellent starting point for the countercurrent or cocurrent model and, therefore, largely alleviates potential problems associated with the limited radius of convergence of our successive substitution method. One could, of course, use more sophisticated numerical techniques, such as the Newton–Raphson approach. However, this approach would require more computation overhead. Typical countercurrent simulations require no more than 5–15 iterations for a four- or five-component mixture, and such a case takes a fraction of a second when the simulator is run using a personal computer.

Cocurrent flow

Figure 3b depicts ideal cocurrent flow in a membrane unit. The modeling approach described for countercurrent flow is followed.

For ideal cocurrent flow, a component j mass balance on stage k is given by

$$\ell_{j,k} + v_{j,k} - \ell_{j,k+1} - v_{j,k+1} = 0 \tag{23}$$

and the mass flow of component j leaving stage k due to permeation is

$$\dot{m}_{j,k} = \ell_{j,k+1} - \ell_{j,k} = Q_j \Delta A_k \left(P_{L_k} \frac{\ell_{j,k}}{L_k} - P_{V_k} \frac{v_{j,k}}{V_k} \right) \tag{24}$$

Equation 24 is rewritten to give the following expression for the permeate flow of component j leaving stage k

$$v_{j,k} = \left(\frac{V_k}{Q_j \Delta A_k P_{V_k}} + \frac{P_{L_k}}{P_{V_k}} \frac{V_k}{L_k} \right) \ell_{j,k} - \frac{V_k}{Q_j \Delta A_k P_{V_k}} \ell_{j,k+1} \tag{25}$$

Equation 25 is combined with Eq. 23 to give an expression for the residue flow leaving stage k

$$\ell_{j,k} = \frac{v_{j,k+1} + \left(1 + \dfrac{V_k}{Q_j \Delta A_k P_{V_k}} \right) \ell_{j,k+1}}{1 + \left(\dfrac{V_k}{Q_j \Delta A_k P_{V_k}} + \dfrac{P_{L_k}}{P_{V_k}} \dfrac{V_k}{L_k} \right)} \tag{26}$$

In applying these coefficients to the first stage (that is, $k = N$), V_N is the sweep flow rate. For component j, Eq. 26 is solved beginning at the feed end of the module ($k = N$) where $\ell_{j,k+1}$ and $v_{j,k+1}$ are known. The calculation proceeds from stage to stage until the residue end of the permeator is reached. The cocurrent case does not require the tridiagonal matrix solution outlined for countercurrent flow. Initial guesses for the overall flow rates and pressures on each stage are provided from the cross-flow model. The calculation of the flow rates of each component on each stage from Eq. 26 provides improved estimates for the total flow rates and pressures, and the calculation is repeated until the change in component flow rates is within a defined tolerance limit. This successive approximation procedure is repeated until

$$\left| \frac{\Delta V_1}{V_1} \right| < 10^{-8} \tag{27}$$

where ΔV_1 is the change in total permeate flow from one iteration to the next.

Table 1. Module and Process Simulation Parameters

	Air Separation	Ternary Separation	H_2 Separation
Feed	Bore	Shell	Shell
Feed Pres. (bara)	10	10	76.9/42.4
Permeate Pres. (bara)	1	1	42.4/7.9
Feed Temp. (°C)	40	25	50
Fiber OD/ID (μm)	300/150	300/150	300/150
Fiber Length (m)	1	1	1
Fiber Pot Length (m)	0.1	0.1	0.1
No. of Fibers	300,000	350,000	500,000
Active Memb. Area (m^2)*	226	264	377

*Active membrane area is calculated as π (Fiber OD)(Fiber Length-2(Fiber Pot Length))(Number of Fibers). The module configuration corresponds to the active separating layer on the exterior of the fiber. The fibers are assumed to be potted on each end.

Results and Discussion

Air separation

The simulation results described in the remainder of this study are for countercurrent contacting. The conditions used for the membrane module are presented in Table 1. For the air separation case, permeances of the membrane to air gases and physical property information related to the air gas components are recorded in Table 2. The membrane permeances are selected to be similar to those which might be observed with a polysulfone membrane with an effective separating layer thickness of approximately 0.1 μm (Anonymous, 1995). In these simulations, the air fed to the module is modeled as a four component mixture of 78.41% nitrogen, 20.84% oxygen, 0.03% carbon dioxide, and 0.72% water (Felder and Rousseau, 1986). The water composition corresponds to saturation at 40°C and ten atmospheres total pressure.

The generation of purified N_2 is an important industrial application of membranes. Several recent patents describe the development of membrane module designs with integral internal purge to simplify the implementation of permeate

Table 2. Permeance and Feed Composition for Air Separation Simulations

Air Separation		
Component	Feed Mole Fraction	Permeance (GPU)*
N_2	0.7841	3.57
O_2	0.2084	20
CO_2	0.0003	60
H_2O	0.0072	1,000

*1 GPU = 10^{-6} cm^3(STP)/($cm^2 \cdot s \cdot$ cm Hg) = 7.501×10^{-12} m^3(STP)/($m^2 \cdot s \cdot$ Pa) = 3.346×10^{-13} kmol/($m^2 \cdot s \cdot$ Pa).

purging (Kalthod, 1996; Nicolas et al., 1995). Nicolas et al. teach a method to prepare a hollow-fiber membrane module with an internal purge valve that may be regulated to vary the amount of the residue or nonpermeate product that is introduced into the permeate stream as a purge (Nicolas et al., 1995). Kalthod teaches a method of permitting permeate purge in a hollow fiber membrane module by shortening some of the hollow fibers in the hollow fiber bundle so that they discharge feed gas directly into the permeate (bore side feed) or so that gas flows directly into the fibers without first permeating through their walls (shell side feed) (Kalthod, 1996). In addition to drying air, Kalthod teaches that purging can improve oxygen production at a fixed oxygen permeate purity.

The effect of permeate purge on nitrogen purity and residue recovery is presented in Figures 4 and 5 for two feed pressures. Residue recovery is the fraction of the feed flow that exits the module in the residue stream. In these simulations, the purge stream is taken from the residue product. Residue recovery is based on residue flow after the purge gas has been removed from the residue stream. A purge level of 10% implies that 10% of the residue gas exiting the module is introduced into the permeate stream on the residue end of the module. Feed flow rate is varied to generate the purity/recovery curves presented in Figure 4. In all cases, as expected, as flow rate is increased (which decreases the gas contact time with the hollow fibers in the module), residue recovery increases (cf. Figure 5) and nitrogen purity decreases (cf. Figure 4). That is, there is a tradeoff between product purity and recovery. For any recovery and any purge level, nitrogen purity increases with increasing feed pressure. (In fact, as discussed in more detail later, it is more appropriate to discuss feed pressure changes in terms of pressure ratio, which is the ratio of feed pressure to permeate pressure. However, when permeate pressure is constant, any change in feed pressure results in a proportional change in pressure ratio, so feed pressure effects in these air separation simulations may be discussed either in terms of feed pressure or pressure ratio.) At higher feed pressure, the driving force for mass transfer is increased and, therefore, the nitrogen purity of the residue is enhanced. From Figure 5, as purge fraction increases at fixed feed pressure and feed flow, overall inerts (that is, residue) recovery decreases, and as upstream pressure increases at fixed purge rate and fixed feed flow, the overall residue recovery is lower. Of course, the lower recovery is accompanied by higher purity as shown in Figure 4.

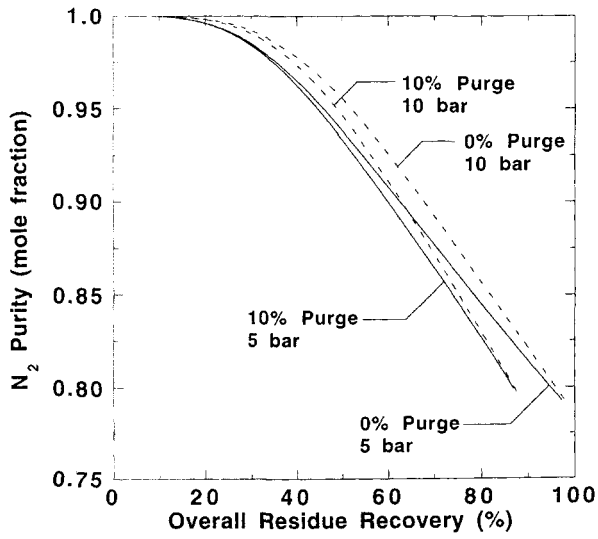

Figure 4. Effect of permeate purge and feed pressure on nitrogen purity in residue.

Solid lines correspond to a feed pressure of 5 bara, and dashed lines correspond to a feed pressure of 10 bara.

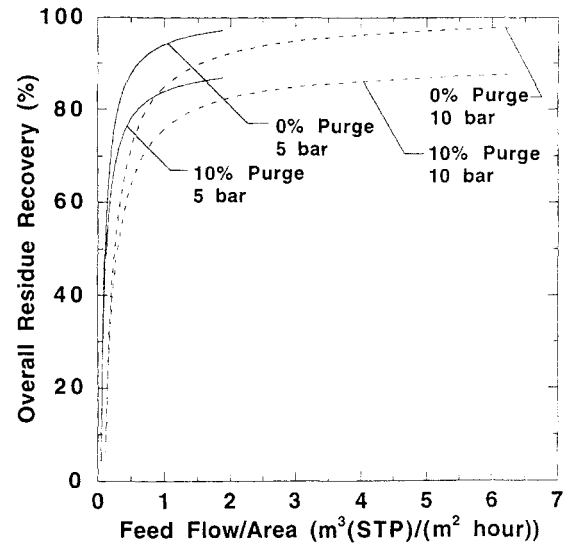

Figure 5. Residue recovery and feed flow as a function of permeate purge and feed pressure.

For producing purified nitrogen, the most advantageous operating conditions are those which yield both high N_2 purity and high N_2 recovery in the residue. As the fraction of the residue gas used for permeate purging increases, there is an unfavorable shift in the nitrogen purity/recovery tradeoff curve (cf. Figure 4). This trend is presented explicitly in Figure 6. In this figure, the effect of permeate purge on residue recovery at fixed purity is presented using two definitions of recovery, R''/F and R'/F. These symbols are depicted in Figure 7. Recovery R''/F is defined based on the residue flow rate at the exit from the hollow-fiber separator. On the other hand, the overall system recovery R'/F is defined based on the residue flow rate after removing the purge stream and represents the amount of residue gas which would be available from this module for downstream uses. In Figures 4 and 5, overall system recovery R'/F is used.

As expected, purging the permeate of a hollow-fiber membrane separator acts to increase the driving force for mass transfer and higher recovery at a fixed residue purity is observed when recovery is based on residue flow rate at the module exit R''/F (Li et al., 1990; Pan and Habgood, 1974; Wang et al., 1992). However, the overall system recovery R'/F decreases due to consumption of potential product gas for the purge (or sweep) stream. As the permeate purge fraction increases, residue recovery at a fixed residue purity would increase, all other factors being equal. However, when the residue stream is used as the source for the purge gas, the performance of the module is penalized by the removal of the purge gas from the residue product. The results in Figure

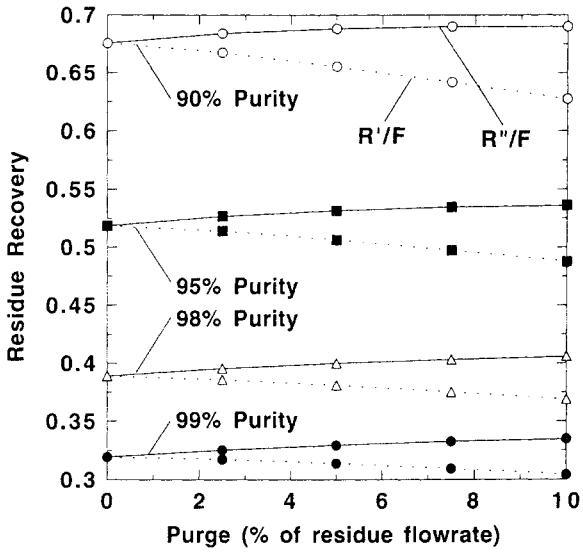

Figure 6. Effect of permeate purge on residue recovery at fixed purity.

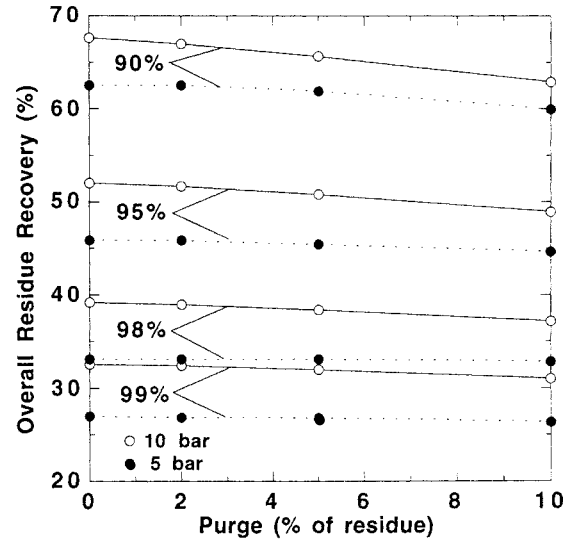

Figure 8. Effect of permeate purge on residue recovery R'/F at fixed nitrogen product purity and fixed feed pressure.

4 indicate that the removal of the purge gas from the residue stream does not provide a sufficient increase in residue recovery in the module to offset the amount of product used for the purge. As a result, overall system residue recovery R'/F at fixed purity is reduced by purging.

The influence of upstream pressure on inerts recovery as a function of purge fraction is presented in Figure 8. At all purity and purge values considered in Figure 8, recovery is higher at higher feed pressure or, equivalently, at higher pressure ratio. Based on the ratio of O_2 and N_2 permeances in Table 2, the O_2/N_2 selectivity is 5.6. The results in Figure 8 were generated at pressure ratios of 5 and 10, values which bracket the membrane selectivity. As demonstrated by Baker and Wijmans (1994), permeate composition increases with increasing pressure ratio and is most sensitive to pressure ratio when selectivity and pressure ratio have similar values. Thus, higher feed pressures increase the efficiency of separation by increasing the pressure ratio, which translates to higher recovery at fixed purity or higher purity at fixed recovery.

The calculations summarized above also yield information about the permeate purity and recovery. The effect of feed pressure and purge fraction on oxygen purity and permeate recovery is presented in Figure 9. Like the nitrogen results, operating at higher pressure improves oxygen purity at a fixed permeate recovery, and purging the permeate with residue gas dilutes the permeate product and results in unfavorable tradeoffs on the purity/recovery map presented in Figure 9. At low permeate recovery values ($< 5\%$ without purging and $< 30\%$ with 10% purging), oxygen purity decreases as recovery decreases. With a tubeside feed module, at very low permeate recoveries, feed flow rates are very high and the transmodule pressure drop in the bore of the hollow fibers becomes large. For example, at 5% permeate recovery, a feed pressure of 10 atmospheres and no purging, the pressure at the residue end of the fibers is only 8.7 atmospheres, a 13% decrease relative to the feed pressure. This large pressure decrease along the length of the fiber results in a lower average driving force for mass transfer which, in turn, leads to lower oxygen purity in the permeate. For cases with purge, the decrease in purity with decreasing permeate recovery (that is, increasing feed flow rate) is exacerbated by the tendency of the higher purge flow rates at higher feed flow rates to dilute the permeate. Of course, as shown in Eq. 21, the feed

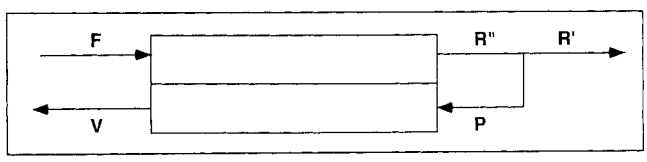

Figure 7. Definitions of recovery for cases with permeate purge.

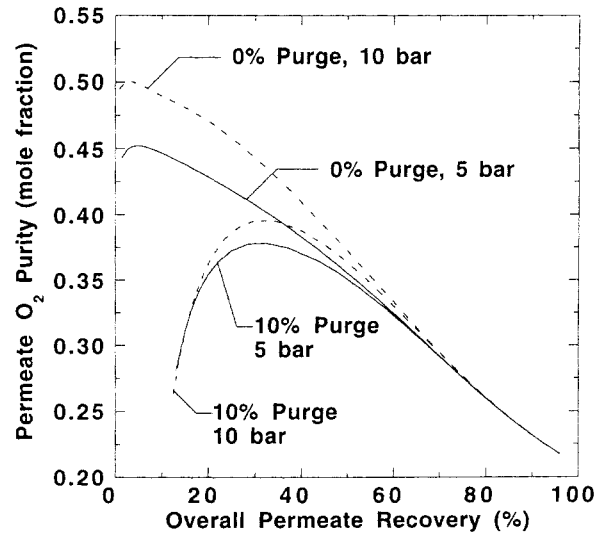

Figure 9. Effect of permeate purge and feed pressure on permeate oxygen purity.

to residue pressure drop is a strong function of fiber inner diameter, and values used for this example are believed to be reasonable based on information describing the state of the art for hollow fibers.

Permeate purging can be used to assist the removal of low concentrations of highly permeable impurities in a feed gas mixture. The use of permeate purging to reduce required membrane area for such applications has been described in general (Pan and Habgood, 1974) and for the removal of CO_2 from sealed life support systems such as submarines and space capsules (Li et al., 1990). Membrane-based air drying is practiced using permeate purging to enhance the rate of removal of water from the feed gas (Wang et al., 1992). The following simulation of air drying demonstrates the effect of purge rate on water removal from air. Figure 10 presents the residue stream dew point temperature as a function of purge fraction for various nitrogen residue purity values and two values of water permeance. The dew point temperature decreases monotonically with increasing purge fraction. As the purge gas is obtained from the residue stream, an increase in purge fraction increases the feed flow to the module to maintain a fixed nitrogen purity, and this increase in feed flow rate decreases the residence time of gas in the module, which tends to increase the concentration of water in the residue and, therefore, the dew point of the residue gas. The residue purge gas also increases the driving force for transport of water, and this tends to decrease the dew point temperature of the product residue gas. The results in Figure 10 suggest that the latter effect is more important than the former, and purging effectively decreases the dew point temperature at fixed nitrogen purity.

High permeability components present in low concentrations, such as water in air, are particularly sensitive to concentration polarization (or mass-transfer limitations) and

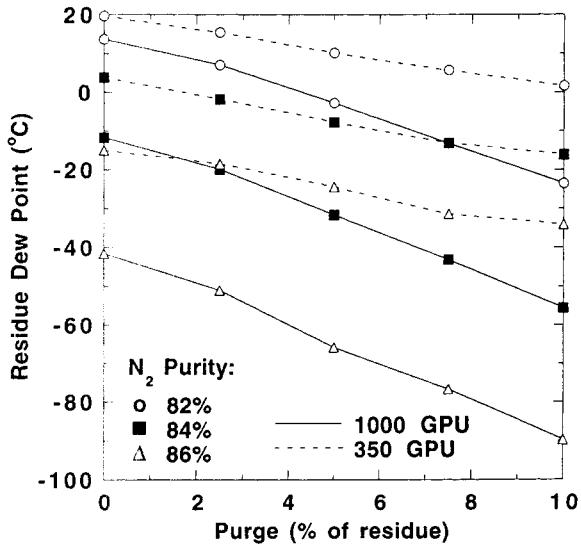

Figure 10. Effect of permeate purging on residue dew point temperature at fixed nitrogen residue purity.

Solid lines correspond to simulations with water permeance of 1,000 GPU and the dashed lines represent simulations with a water permeance of 350 GPU. Other module and membrane parameters are recorded in Tables 1 and 2.

shell-side fluid flow maldistribution (Wang et al., 1992). These factors act to decrease the efficiency of the separator for removing such components from the feed gas. To provide a rough qualitative guide of the influence of such effects on the results just presented, we have recomputed these results using an effective water permeance of 350 GPU rather than 1,000 GPU. These results are also presented in Figure 10 as dashed lines. As expected, the residue dew point is higher when the water permeance is lower. Moreover, the effect of purging on residue dew point temperature is weaker when water permeance is lower. For example, at 86% N_2 purity, 10% purge decreases the dew point by nearly 50°C from −41.6°C to −89.7°C. In contrast, when the effective water permeance is only 350 GPU, the dew point decreases by less than 20°C, from −15.0°C to −34.1°C, as the purge is increased from 0 to 10% of the residue flow rate at 86% residue N_2 purity.

Hydrogen separation

Hydrotreatment is a common unit operation in refineries. In this process, petroleum intermediates are contacted with hydrogen under appropriate conditions to reduce the sulfur, nitrogen, metals, asphaltene, and carbon residue content of the feedstock. This process requires substantial amounts of hydrogen gas, and much of the excess hydrogen is available for recycle. Membranes are often used to purify the recycled hydrogen. The major impurities are light hydrocarbons. The composition of a typical feedstream to a membrane hydrogen purification from a hydrotreater is given in Table 3. For the simulations described below, the membrane permeance values are roughly those expected for a polysulfone membrane with an 0.1 μm thick effective separating layer (Anonymous, 1995).

The hydrogen product produced by the membrane is in the permeate stream, so the purified hydrogen is available at lower pressure than the feed. The permeate pressure is an important process variable since the utility of the hydrogen produced by the membrane process depends, in part, on the pressure at which the hydrogen is produced. Generally, the hydrogen produced in the permeate stream is more valuable or useful if it is produced at higher permeate pressure to minimize or avoid recompression costs.

To illustrate the effect of pressure or, more appropriately, pressure ratio on hydrogen purity and recovery, two cases are presented in Figure 11. The simulation parameters used for this separation are provided in Tables 1 and 3. Feed flow rate is varied to obtain results at various purity/recovery values. In both cases, the pressure difference between the feed

Table 3. Permeance and Feed Composition for Hydrogen Separation Simulations

Hydrogen Separation		
Component	Feed Mole Fraction	Permeance (GPU)
H_2	0.650	100
C_2H_4	0.025	3.03
CH_4	0.210	2.86
C_2H_6	0.080	2.00
C_3H_8	0.035	1.89

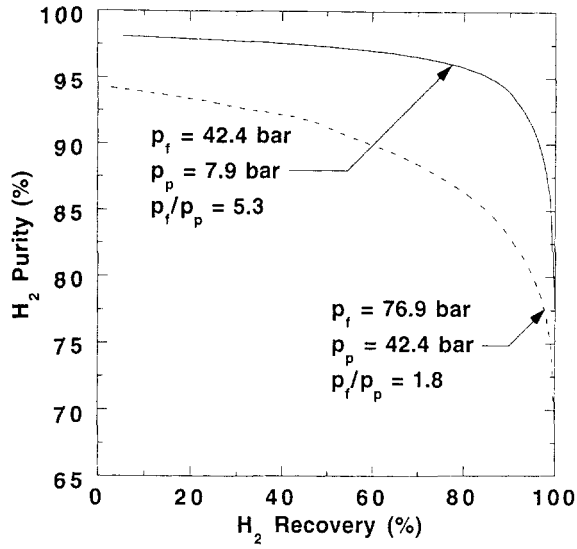

Figure 11. Influence of pressure ratio on hydrogen purity/recovery characteristics in hydrotreater applications.

The pressure difference between the feed and permeate pressure is maintained constant at 34.7 bar (500 psi). In this figure, p_f is the feed pressure, and p_p is the permeate pressure (Pa).

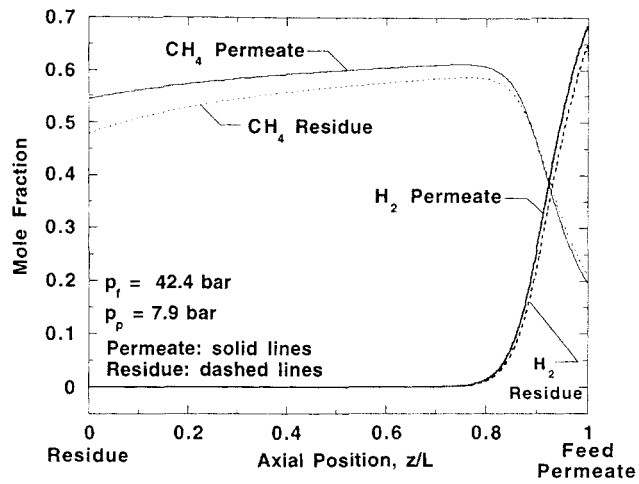

Figure 12. Hydrogen and ethylene concentration profiles in hydrotreater application.

In this figure, p_f is the feed pressure, and p_p is the permeate pressure (Pa). The feed flow rate is 283.2 m^3(STP)/h (10,000 SCFH), and the total permeate recovery is 94.6%.

and permeate streams is maintained constant at 34.7 bar (500 psi). However, the ratio of feed to permeate pressure is quite different for the two cases, 5.3 when the feed pressure is 42.4 bar and 1.8 when the feed pressure is 76.9 bar. When the pressure ratio is higher, hydrogen recovery is higher at each hydrogen purity or, alternatively, hydrogen purity in the permeate is higher at any recovery even though absolute feed pressure is lower. However, this improvement in separation performance comes at a penalty, since the permeate pressure is lower in the higher-pressure ratio case and would, therefore, result in more recompression costs if the H_2 needed to be supplied to a downstream process or recycled at, for example, the feed pressure. These results suggest a complex economic tradeoff between compression costs, hydrogen recovery, and hydrogen purity that is probably rather unique to each hydrogen application.

Concentration profiles for two components, hydrogen and methane, are presented as a function of axial position in the module in Figure 12. In this figure, z/L is the normalized axial coordinate in the module, and L is the active fiber length, which is the total fiber length (1 m) less than the length of the potted ends of the fibers (0.2 m). The residue end of the module is at $z = 0$, and $z = L$ corresponds to the feed and permeate end of the module (see Figure 1). The concentration profiles are presented for a case which exhibits extremely high permeate recovery (94.6%). As expected, the composition of hydrogen decreases rapidly from the feed end of the module (that is, $z/L = 1$) where most of the hydrogen is stripped from the feed and appears in the permeate. (At this high recovery, only about 20% of the module membrane area is efficiently used for H_2 purification.) While this recovery is higher than one would typically find in industrial practice, this case serves to illustrate the following two points. First, the composition of methane, a component of intermediate permeability in this mixture, exhibits a maximum with axial position. Such maxima were not observed in the binary case and prompted further simulation studies of a ternary mixture to probe the observed maxima in composition profiles. Secondly, the hydrogen concentration on both the high- and low-pressure sides of the membranes becomes very small near the residue end of the fibers. In the region where the hydrogen concentration profile appears flat in Figure 12 ($0 \leq z/L < 0.75$), the hydrogen partial pressure is practically equal on both the high- and low-pressure sides of the fibers. In tests we ran using shooting methods to solve the governing differential equations, we found the numerical methods to be unstable and were unable to achieve convergence in such cases. Therefore, this case also illustrates the robustness of the model for simulation conditions at very high recovery when an extremely permeable component is removed to such an extent that the partial pressures on both the high- and low-pressure side of the membrane become practically equal. One would expect this situation to occur rather frequently in dehydration applications since water is usually much more permeable than any other component in the mixture.

Model three component separation

A ternary case was selected for studies of the maxima in composition profiles because this is the simplest case which, with constant permeability coefficients, can exhibit the maxima in compositions seen in the five component refinery case. The simulation conditions are presented in Tables 1 and 4. We have selected an equimolar feed mixture with a maximum selectivity of 50. Typical composition profiles are presented in Figure 13 for a feed flow rate of 283.2 m^3 (STP)/h (10,000 SCFH). The residue and permeate composition of the most permeable component (that is, component 1) decreases as z/L (that is, distance from the residue end of the permeator) decreases since this component is most efficiently stripped from the feed. The residue and permeate compositions of component 3, the least permeable component, increase monotonically as z/L decreases, which reflects the

Table 4. Permeance and Feed Composition for Ternary Separation Simulations

Ternary Separation		
Component	Feed Mole Fraction	Permeance (GPU)
1	0.3333	500
2	0.3333	100
3	0.3334	10

systematic enrichment of the residue stream in this component (due to selective removal of the other more permeable species) as distance from the feed end of the permeator increases. The residue and permeate compositions of component 2, whose permeability is intermediate between that of the other components, exhibit a maximum. In a mixture of two components, the composition of the more permeable component always increases in the permeate and residue as the distance from the closed (that is, residue) end of the fibers is increased and *vice versa* for the less permeable component. In a three-component mixture, a very permeable component will be largely removed from the feed in a relatively short distance from the feed end of the fibers, which will increase the composition of the remaining two components in the residue. Then, the composition of the second most permeable component must begin to decrease as this component is selectively removed from the residue, and the composition of the least permeable component will continue to increase over the entire length of the fibers. In this way, in mixtures with at least three components, maxima in the compositions of components of intermediate composition may be observed. Staging of membrane modules in series could be used to harvest components of intermediate permeability at maximum concentration.

Conclusions

A model for multicomponent gas separation using a hollow-fiber contactor is presented. The model permits simulation of cocurrent, countercurrent, and cross-flow contacting patterns with permeate purging (or sweep). Examples of use of the model are provided by three separate case studies. In air separation, permeate purging using a fraction of the residue stream is shown to be an inefficient means to improve nitrogen or oxygen purity. However, for air drying, purging the permeate with a small fraction of the residue stream can markedly reduce the dew point of the residue stream. In 3+ component mixtures, maxima in the composition of components of intermediate permeability may be observed.

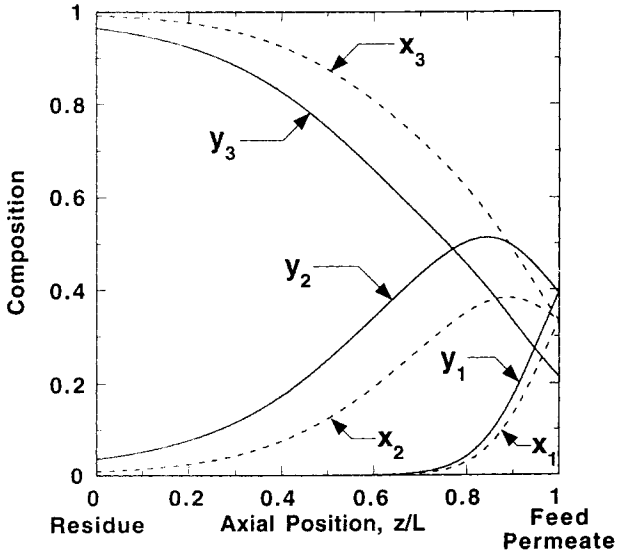

Figure 13. Residue (x_i) and permeate (y_i) concentration profiles in ternary case.

Acknowledgments

The authors gratefully acknowledge partial support of this work from the National Science Foundation (CTS-9257911 (NSF Young Investigator Award-BDF)). One of the authors (BDF) benefited significantly from conversations with Dr. Steve Auvil of Air Products and Chemicals, Inc., Allentown, PA, regarding membrane-based air drying.

Notation

F = total feed flow rate (kmol/s)
ΔL_k = difference in total residue flow rate on stage k between two iterations (kmol/s)
R'' = total residue flow rate from module (kmol/s)
R' = total residue flow rate after removing purge stream (kmol/s)
V = total permeate flow rate (kmol/s)
ΔV_k = difference in total permeate flow rate on stage k between two iterations (kmol/s)
x_{F_j} = feed mole fraction of component j
z = axial distance along the active section of the hollow fibers measured from the residue end of the module, m

Literature Cited

Anonymous, *Permeability and Other Film Properties*, Plastics Design Library, New York (1995).
Baker, R. W., and J. G. Wijmans, "Membrane Separation of Organic Vapors from Gas Streams," *Polymeric Gas Separation Membranes*, D. R. Paul and Y. P. Yampol'skii, eds., CRC Press, Boca Raton, FL, p. 353 (1994).
Baker, R. W., N. Yoshioka, J. M. Mohr, and A. J. Khan, "Separation of Organic Vapors from Air," *J. Memb. Sci.*, **31**, 259 (1987).
Barrer, R. M., J. A. Barrie, and N. K. Raman, "Solution and Diffusion in Silicone Rubber: I. A Comparison with Natural Rubber," *Polymer*, **3**, 595 (1962).
Basaran, O. A., and S. R. Auvil, "Asymptotic Analysis of Gas Separation by a Membrane Module," *AIChE J.*, **34**, 1726 (1988).
Bird, R. B., W. E. Stewart, and E. N. Lightfoot, *Transport Phenomena*, Wiley, New York (1960).
Bollinger, W. A., S. P. Long, and T. R. Metzer, "Optimizing Hydrocracker Hydrogen," *Chem. Eng. Prog.*, **80**(5), 51 (1984).
Boucif, N., S. Majumdar, and K. K. Sirkar, "Series Solutions for a Gas Permeator with Countercurrent and Cocurrent Flow," *Ind. Eng. Chem. Fundam.*, **23**, 470 (1984).
Felder, R. M., and R. W. Rousseau, *Elementary Principles of Chemical Processes*, 2nd ed., Wiley, New York (1986).
Freeman, B. D., and I. Pinnau, "Separation of Gases Using Solubility-Selective Polymers," *Trends in Poly. Sci.*, **5**, 167 (1997).
Geankoplis, C. J., *Transport Processes and Unit Operations*, 3rd ed., Prentice Hall, Englewood Cliffs, NJ, p. 921 (1993).
Ghosal, K., and B. D. Freeman, "Gas Separation Using Polymer Membranes: An Overview," *Poly. for Adv. Technol.*, **5**, 673 (1994).
Graham, T., "On the Absorption and Dialytic Separation of Gases by Colloid Septa: I. Action of a Septum of Caoutchouc," *Phil. Mag.*, **32**, 401 (1866).
Kalthod, D. G., "Production of Enriched Oxygen Gas Stream Utilizing Hollow Fiber Membranes," U.S. Patent 5,500,036, assigned to Air Products and Chemicals, Inc. (1996).
King, C. J., *Separation Processes*, 2nd ed., McGraw Hill, New York, p. 466 (1980).

Kovvali, A. S., S. Vemury, K. R. Krovvidi, and A. A. Khan, "Models and Analyses of Membrane Gas Permeators," *J. Memb. Sci.*, **73**, 1 (1992).
Krovvidi, K. R., A. S. Kovvali, S. Vermury, and A. A. Khan, "Approximate Solutions for Gas Permeators Separating Binary Mixtures," *J. Memb. Sci.*, **66**, 103 (1992).
Li, K., D. R. Acharya, and R. Hughes, "Membrane Gas Separation with Permeate Purging," *Gas Sep. and Purif.*, **4**(2), 81 (1990).
Lipscomb, G. G., "Design of Hollow Fiber Contactors for Membrane Gas Separations," *The 1996 Memb. Technol. Rev.*, D. Mulloy, ed., Business Communications Co., Norwalk, CT, p. 23 (1996).
Maclean, D. L., C. E. Prince, and Y. C. Chae, "Energy Saving Modifications in Ammonia Plants," *Chem. Eng. Prog.*, **76**, 98 (1980).
Morisato, A., H. C. Shen, S. S. Sankar, B. D. Freeman, I. Pinnau, and C. G. Casillas, "Polymer Characterization and Gas Permeability of Poly(1-Trimethylsilyl-1-Propyne) [PTMSP], Poly(1-Phenyl-1-Propyne) [PPP], and PTMSP/PPP Blends," *J. Poly. Sci.: Poly. Phys. Ed.*, **34**, 2209 (1996).
Naylor, R. W., and P. O. Backer, "Enrichment Calculations in Gaseous Diffusion: Large Separation Factor," *AIChE J.*, **1**, 95 (1955).
Nicolas, P. S., B. Bikson, S. Giglia, and D. R. Thompson, "Fluid Separation Assembly Having an Purge Control Valve," U.S. Patent 5,411,662, assigned to Praxair Technology, Inc. (1995).
Pan, C. Y., "Gas Separation by High-Flux Asymmetric Hollow-Fiber Membrane," *AIChE J.*, **32**, 2020 (1986).
Pan, C. Y., and H. W. Habgood, "An Analysis of the Single-Stage Gaseous Permeation Process," *Ind. Eng. Chem., Fundam.*, **13**, 323 (1974).
Shindo, Y., T. Hakuta, H. Yoshitome, and H. Inoue, "Calculation Methods for Multicomponent Gas Separation by Permeation," *Sep. Sci. and Tech.*, **20**, 445 (1985).
Smith, S. W., B. D. Freeman, C. K. Hall, and R. Rautenbach, "Analytical Gas-Permeation Models for Binary Gas Mixture Separation Using Membrane Modules," *J. Memb. Sci.*, **118**, 289 (1996).
Spillman, R. W., "Economics of Gas Separation Membranes," *Chem. Eng. Prog.*, **85**(1), 41 (1989).
Wang, K. L., S. H. McCray, D. D. Newbold, and E. L. Cussler, "Hollow Fiber Air Drying," *J. Memb. Sci.*, **72**, 231 (1992).
Weller, S., and W. A. Steiner, "Fractional Permeation Through Membranes," *Chem. Eng. Prog.*, **46**, 585 (1950).
Zolandz, R. R., and G. K. Fleming, "Gas Permeation," *Membrane Handbook*, W. S. W. Ho and K. K. Sirkar, eds., Van Nostrand Reinhold, New York, p. 17 (1992).

Appendix: Mechanical Energy Balance to Calculate Shell Side Pressure Drop

The Hagen-Poiseuille relation is most often used to calculate shell side pressure variations in hollow fiber gas separation simulations (Kovvali et al., 1992; Lipscomb, 1996). Strictly speaking, this relation (Eq. 21) is only valid for steady-state, laminar, incompressible flow of a Newtonian fluid in a circular pipe with impermeable walls. In this appendix, we use the steady-state mechanical energy balance to derive a more general result for pressure changes in a permeable hollow fiber of constant radius R_i, through which a compressible gas flows. This result is then used to identify the criteria for which the Hagen-Poiseuille relation would not provide an adequate description of the pressure distribution in the hollow fiber.

Figure A1 presents a cross-sectional view of stage k of a hollow fiber of length Δz. In this figure, high-pressure gas permeates from the interior to the exterior of the fiber. This corresponds to a bore side feed case. Modification of the derivation below for shell side feed is obvious.

The steady-state, isothermal mechanical energy balance for gas in plug flow through the section of hollow fiber in Figure A1 is given by (Bird et al., 1960)

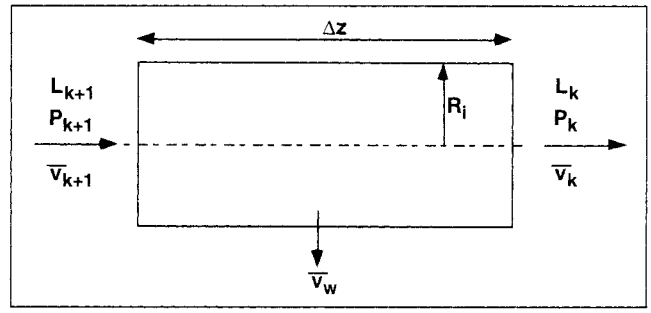

Figure A1. Cross-sectional view of stage k section of hollow fiber.

$$L_{k+1}\left[\frac{1}{2}\bar{v}_{k+1}^2+\int_{P_o}^{P_{L_{k+1}}}\hat{V}dP\right]-L_k\left[\frac{1}{2}\bar{v}_k^2+\int_{P_o}^{P_{L_k}}\hat{V}dP\right]$$
$$-(L_{k+1}-L_k)\left[\frac{1}{2}\bar{v}_w^2+\int_{P_o}^{P_{L_k}}\hat{V}dP\right]=\frac{1}{2}\bar{v}_k^2L_k\frac{\Delta z}{R_i}f \quad \text{(A1)}$$

where $\bar{v}_{k+1}$, $\bar{v}_k$, and $\bar{v}_w$ are the average velocities of gas entering stage k (m/s) from the previous stage, leaving stage k for the next stage, and leaving stage k as a result of permeation through the wall of the hollow fiber. P_o is a reference pressure, $\hat{V}$ is the specific volume of the gas mixture (m^3/kg), f is the Fanning friction factor, and Δz ($= L/N$) is the length of stage k. As the gas flow rates encountered in the simulations discussed in this article are in the laminar flow regime, the friction factor is given by (Bird et al., 1960)

$$f=\frac{16}{Re}=\frac{16\mu_{\text{mix}}\hat{V}}{2R_i\bar{v}_k}=\frac{8\mu_{\text{mix}}\hat{V}}{R_i\bar{v}_k} \quad \text{(A2)}$$

If situations other than laminar flow are of interest, the appropriate relation between the friction factor and the Reynolds number may be introduced as needed. We restrict our analysis to ideal gases, for which the specific volume is given by (Bird et al., 1960)

$$\hat{V}=\frac{RT}{MP} \quad \text{(A3)}$$

where M is the mole-fraction weighted molecular weight (kg/kmol) of the gas mixture, T is the absolute temperature (K), R is the gas constant [$m^3\cdot$Pa/(kmol)$\cdot$K], and P is pressure (kmol/s). This assumption may, of course, be relaxed by introducing another equation of state to describe the relationship between temperature, pressure, and gas specific volume.

The average axial velocity may be written as follows

$$\bar{v}_k=\frac{L_k\text{RT}}{AP_{L_k}}=\frac{L_k\text{RT}}{\pi R_i^2P_{L_k}} \quad \text{(A4)}$$

where A is the cross-sectional area of the fiber (πR_i^2).

Inserting Eqs. A4, A3, and A2 into A1, carrying out the required integrations, and combining terms, the following ex-

pression, which describes the pressure distribution in the bore of the hollow fibers, is obtained

$$\ln\frac{P_{L_{k+1}}}{P_{L_k}} = \frac{8\mu_{\text{mix}}}{R_i^2}\frac{\bar{v}_k}{P_{L_k}}\frac{L_k}{L_{k+1}} + \frac{\text{RT}}{2\text{M}}\frac{(L_k/A)^2}{P_{L_k}^2} \times\left[\frac{L_k}{L_{k+1}} - \left(\frac{P_{L_k}}{P_{L_{k+1}}}\right)^2\right] + \frac{M}{2\text{RT}}\bar{v}_w^2\frac{[L_{k+1}-L_k]}{L_{k+1}} \quad \text{(A5)}$$

The first term on the righthand side of Eq. A5 represents the contribution of viscous forces to pressure changes in the fiber, the second term corresponds to the effect of gas compressibility on pressure changes, and the last term describes the impact of loss (or gain) of gas due to permeation of gas through the fiber walls in bore side (or shell side) feed.

If the second and third terms on the righthand side of Eq. A5 are negligible, then Eq. A5 reduces to the Hagen–Poiseuille relation in Eq. 21. Equation A5 may be used in place of Eq. 21 to compute the pressure profile in each stage of the hollow fiber module. Unlike the Hagen–Poiseuille equation, Eq. A5 requires an iterative solution procedure. The Hagen–Poiseuille relation should provide an excellent initial guess for the iteration process.

In the following sections, we derive expressions for the conditions under which gas compressibility and gas loss due to permeation through the hollow fibers are negligible relative to viscous forces. The results are expressed in terms of dimensionless numbers, which can easily be calculated to determine the relative importance of each term in Eq. A5.

Influence of Gas Compressibility on Pressure Profile

To determine the criteria under which gas compressibility effects are insignificant, we first simplify Eq. A5. We neglect the influence of gas loss (or gain) through the permeable fiber walls (that is, we neglect the last term in Eq. A5). We then consider a section of fiber short enough so that $L_k \approx L_{k+1}$ and that the lefthand side of Eq. A5 may be expanded in a Taylor series to give

$$\Delta P = -\frac{8\mu_{\text{mix}}\bar{v}_k}{R_i^2}\Delta z - \frac{\text{RTM}}{2}\frac{(L_k/A)^2}{P_{L_k}}\left[1-\left(\frac{P_{L_k}}{P_{L_{k+1}}}\right)^2\right] \quad \text{(A6)}$$

where the pressure change across the section of the hollow fiber ΔP is $\Delta P = P_{L_k} - P_{L_{k+1}}$. When the section of the hollow fiber is short, the term in brackets on the righthand side of Eq. A5 may be expanded in a Taylor series as follows

$$1-\left(\frac{P_{L_k}}{P_{L_{k+1}}}\right)^2 = -2\frac{\Delta P}{P_{L_{k+1}}} \quad \text{(A7)}$$

Inserting Eq. A7 into A6 and rearranging yields

$$\Delta P = -\frac{8\mu_{\text{mix}}\bar{v}_k/R_i^2}{\left[1-\text{RTM}\dfrac{(L_k/A)^2}{P_{L_k}P_{L_{k+1}}}\right]}\Delta z \quad \text{(A8)}$$

Clearly, gas compressibility effects will be negligible when the following criterion is met. (For the purpose of this analysis, it is appropriate to introduce the approximation: $P_{L_{k+1}} \approx P_{L_k}$.)

$$\frac{P_{L_k}^2}{\text{RTM}(L_k/A)^2} \gg 1 \quad \text{(A9)}$$

In the simulations described in this article, a high value of feed gas flow rate to a module containing 300,000 fibers would be 283.2 m^3(STP)/h (10,000 SCFH). This corresponds to a maximum flow rate per fiber L_k of 2.62×10^{-7} m^3 (STP)/s or 1.17×10^{-8} kmol/s. If the fibers have an inside radius of 75 $\times10^{-6}$ m, the cross-sectional area A is 1.77×10^{-8} m^2. The temperature is 323 K, the highest used in our simulations, the pressure is one bara (the lowest value used in our simulations), and the gas molecular weight is 44 kg/kmol, the highest value used in the simulations. The flow rate per unit area L_k/A is 0.661 kmol/(m^2·s). With these values, the numerical value of the term in Eq. A8 is 200, which is much greater than one. The values used in this example were selected to provide a conservative (that is, low) value of the term in Eq. A9. This result means that viscous effects are 200 times more important than gas compressibility effects on the axial pressure profile for this case. Therefore, for all of the cases which we have considered, gas compressibility effects are negligible.

Influence of Fiber Wall Permeability on Pressure Profile

To evaluate the influence of fiber wall permeability on the pressure profile, we use the approach outlined in the previous section, that is, we evaluate the importance of the permeable fiber contribution to Eq. A5 relative to that of viscous forces. Neglecting the gas compressibility term and choosing a short enough section of fiber such that the Taylor series expansion of the lefthand side of Eq. A5 is valid, we obtain

$$\frac{\Delta P}{P_{L_k}} = -\frac{8\mu_{\text{mix}}}{R_i^2}\frac{\bar{v}_k}{P_{L_k}}\frac{L_k}{L_{k+1}}\Delta z - \frac{M}{2\text{RT}}\bar{v}_w^2\frac{[L_{k+1}-L_k]}{L_{k+1}} \quad \text{(A10)}$$

The average velocity of gas exiting or entering the fiber wall due to permeation is

$$\bar{v}_w = [L_{k+1}-L_k]\frac{\text{RT}}{P_{L_k}A_w} \quad \text{(A11)}$$

where A_w is the active area for permeation through the fiber wall and is taken to be $2\pi R_o\Delta z$, consistent with Eq. 1 and the fact that the separation membrane is typically on the outside of the hollow fiber. The difference in flow rate at the entrance and exit of the fiber is due to permeation through the fiber wall and, using Eq. 8, can be written as follows

$$L_{k+1} - L_k = A_w\sum_{j=1}^{R}\dot{m}_{j,k} \quad \text{(A12)}$$

For convenience, we define the pressure-normalized total permeance Q [kmol/(m^2·s·Pa)] as follows

$$Q = \frac{\sum_{j=1}^{R} \dot{m}_{j,k}}{P_{L_k}} \tag{A13}$$

Introducing Eqs. A11, A12, and A13 into Eq. A10, we obtain

$$\frac{\Delta P}{P_{L_k}} = -\left[\frac{8\mu_{\text{mix}}}{R_i^2}\frac{\bar{v}_k}{P_{L_k}}\frac{L_k}{L_{k+1}} + \frac{\pi \text{MRTQ}^3 P_{L_k}}{L_{k+1}}\right]\Delta z \tag{A14}$$

Clearly, the influence of wall permeation on the pressure profile inside the fibers will be negligible when the first term inside the brackets of Eq. A14 is much larger than the second term

$$\frac{8\mu_{\text{mix}}}{R_i^2}\frac{\bar{v}_k}{P_{L_k}}\frac{L_k}{L_{k+1}} \gg \frac{\pi \text{MRTQ}^3 P_{L_k}}{L_{k+1}} \tag{A15}$$

Inserting Eq. A4 into A15 and rearranging, we arrive at the criteria for which permeation through the fiber walls makes a negligible contribution to the pressure profile inside the hollow fibers

$$\frac{8}{\pi^2}\frac{\mu_{\text{mix}}}{R_i^4 R_o}\frac{L_k^2}{M}\frac{1}{(QP_{L_k})^3} \gg 1 \tag{A16}$$

As an example calculation representative of our simulations, we take the gas viscosity to be 2×10^{-5} Pa·s (0.02 cp) and the fiber inner radius to be the same as in the previous example 75×10^{-6} m. The gas molecular weight is 2 kg/kmol, that of hydrogen, one of the most permeable components considered in our study. We use the maximum value of pressure 76.9 bara, and outer radius is 150×10^{-6} m. The value of Q is taken to be 100 GPU (3.346×10^{-10} kmol/(m^2·s·Pa)), which corresponds to the maximum value of this function if we treat the feed gas to be pure hydrogen and allow the permeate pressure to be zero. Basically, setting Q to this large value and using the highest feed pressure considered in this study and zero permeate pressure maximizes the amount of gas which can permeate through the fiber wall. With these values, we find that the lefthand side of Eq. A16 is 1.4×10^7, which is much greater than one. This result means that pressure changes due to viscous losses are roughly 14,000,000 times as large as pressure changes due to permeation through the fiber walls. Even at feed flow rates orders of magnitude less than those considered in this example, the gas permeability effect on the bore side pressure profile would be negligible.

In this Appendix, we have derived the criteria to determine whether or not gas compressibility and fiber permeability influence the pressure profile in the bore of the hollow fibers. In all cases considered in this article, these effects are negligible and the pressure distribution should, therefore, be well-represented by the Hagen–Poiseuille equation.

Manuscript received Dec. 10, 1997, and revision received Feb. 26, 1998.